Zero-Dimensional Cs_3BiX_6 (X = Br, Cl) Single Crystal Films with Second Harmonic Generation

Junjie Yao[1,2†], Zhicheng Zhou[1†], Lutao Li[1†], Yuan Chen[2*], Chen Wang[2], Xiangyi Wang[1], Zheng Lu[1], Zhongchao Bai[2], Qiang Zhang[2], Xuefeng Huangfu[3], Yinghui Sun[1], Hao Xu[3,4] and Guifu Zou[1*]

Abstract

The development of atomically thin single crystal films is necessary to potential applications in the 2D semiconductor field, and it is significant to explore new physical properties in low-dimensional semiconductors. Since, zero-dimensional (0D) materials without natural layering are connected by strong chemical bonds, it is challengeable to break symmetry and grow 0D Cs_3BiX_6 (X = Br, Cl) single crystal thin films. Here, we report the successful growth of 0D Cs_3BiX_6 (X = Br, Cl) single crystal films using a solvent evaporation crystallization strategy. Their phases and structures are both well evaluated to confirm 0D Cs_3BiX_6 (X = Br, Cl) single crystal films. Remarkably, the chemical potential dependent morphology evolution phenomenon is observed. It gives rise to morphology changes of Cs_3BiBr_6 films from rhombus to hexagon as $BiBr_3$ concentration increased. Additionally, the robust second harmonic generation signal is detected in the Cs_3BiBr_6 single crystal film, demonstrating the broken symmetry originated from decreased dimension or shape change.

Keywords: Zero-dimensional, Cs_3BiBr_6, Cs_3BiCl_6, Single crystal film, Second harmonic generation

Introduction

Zero-dimensional (0D) inorganic perovskites offer a unique opportunity to investigate and decipher the charge carrier behavior in an intrinsically strong quantum-confined environment [1]. These reduced-dimensional perovskites have attracted a growing number of experimental and theoretical research groups around the world because of their high thermal and chemical stability as compared to their 3D analogues [2]. Atomically thin single crystal films have shown prospective applications in two-dimensional (2D) semiconductor device fields, such as field effect transistors, [3] photodetectors [4–7], phototransistors [8], light emitting diodes, [9, 10] laser diodes, [11] resistive random access memories, [12, 13] etc. Some novel physical properties can be observed upon the reduction of crystalline dimensions. For instance, Ciarrocchi et al. [14] reported the transition from metal to semiconductor by modulating thickness of transition metal dichalcogenides. Zhang et al. [15] revealed the transition from direct band gap to indirect band gap in atomically thin Arsenene and Antimonene. Wang et al. [16] observed the increased superconducting Curie temperature in high-quality monolayer superconductor $NbSe_2$ grown by chemical vapor deposition. Cheema et al. [17] addressed the enhanced ferroelectricity in ultrathin-doped hafnium oxide grown directly on silicon. Huang et al. [18] studies the layer-dependent ferromagnetism in a van der Waals crystal down to the monolayer limit. Zhang et al. [19] have the experimental observation of the quantum Hall effect and Berry's phase in graphene. Therefore, it is of great significance to develop new atomic layer semiconductor single crystal films [20–24].

[†]Junjie Yao, Zhicheng Zhou and Lutao Li contribute equally

*Correspondence: chenyuan@njust.edu.cn; zouguifu@suda.edu.cn

[1] School of Energy, Key Laboratory of Advanced Carbon Materials and Wearable Energy Technologies of Jiangsu Province, Soochow University, Suzhou 215006, People's Republic of China
[2] College of Mechanical and Electronic Engineering, Shandong University of Science and Technology, Qingdao 266590, People's Republic of China
Full list of author information is available at the end of the article

Yao *et al. Nanoscale Research Letters*   (2022) 17:115

Page 2 of 9

In recent years, halide perovskites have drawn attentions due to their excellent light absorption coefficient, low trap state density, high carrier mobility, long carrier diffusion distance, as well as high defect tolerance factor [25–28]. It has been widely recognized as one of the most promising materials in future optoelectronic field. Inspired by the tremendous progress of 2D semiconductors, researchers spare much effort to explore their dimension dependent properties, [29–35] especially when its thickness is reduced to atomically thin [3, 26, 36, 37]. Currently, the atomically thin single crystal films of lead halide perovskites have been intensively investigated, including cubic, orthorhombic, and Ruddlesden–Popper structures [38–41]. As well known, the lead-free perovskites are one of the most important branches in the perovskites family due to environmental friendly and higher stability as well as excellent optoelectronic properties. [29, 30, 42, 43] Particularly for the Bi-based perovskites derivatives, [44–46] $Cs_3Bi_2X_9$ has been demonstrated the potential applications for solar cells, light emitting diodes, photodetectors, etc. Although the Cs_3BiX_6 bulk and quantum dots have been synthesized and employed for x-ray scintillation and photodetectors, [47–50], there is still few report focused on the growth of Cs_3BiX_6 (X = Br, Cl) single crystal films.

Here, we report the growth of zero-dimensional Cs_3BiX_6 (X = Br, Cl) single crystal films using a solvent evaporation crystallization strategy. Their phase and structures are well evaluated to confirm zero-dimensional Cs_3BiX_6 (X = Br, Cl) single crystal films. It is revealed that the chemical potential dependent morphology evolution phenomenon makes the morphology of Cs_3BiBr_6 film change from rhombus to hexagon, as the $BiBr_3$ concentration increased. A robust second harmonic generation signal was observed in the Cs_3BiBr_6 single crystal film, which demonstrated the broken symmetry due to decreased dimension or shape change. This work not only provides a single crystal film growth method for zero-dimensional structural materials, but also conducive to understanding the electron and band structure change as thickness reduced. This cross-disciplinary research represents a remarkable advance in nanomaterials science, chemistry and crystal growth.

Experiment Details
Grown of Atomically Thin Cs_3BiBr_6 and Cs_3BiCl_6 Single Crystal Films
The thin Cs_3BiBr_6 single crystal film is synthesized from a drop casting and solvent evaporation crystallization process. The substrate for the films growing is Si/SiO2, briefly, 15 mM CsBr and 10 mM $BiBr_3$ are firstly dissolved in 1 mL dimethyl sulfoxide, then, 0.1 mL *n*-octanoic acid is added and mixing uniformly. Subsequently, 20 µL

above transparent solution is dropped onto cleaned SiO_2/ Si substrate and heated to 80 ℃ for 30 min, as the solution reach supersaturation, the nucleation and growth occurs. Finally, the films are produced on the substrate. For the Cs_3BiCl_6 single crystal film growth, all of the procedures are kept the same as Cs_3BiBr_6 film, only replace the CsBr and $BiBr_3$ with CsCl and $BiCl_3$, respectively.

Characterization
Optical microscopy images are taken using a Nikon ECLIPSE LV150N microscopy; SEM images are taken using a Hitachi (SU-8010) which equipped with a x-ray energy dispersion spectra; TEM images are recorded from (F20, 200 kV); X-ray diffraction pattern is taken in x-ray diffractometer (Bruker D8 Advance); XPS patterns are taken in x-ray photoelectron spectroscopy (THERMO FISHER, ESCALAB 250Xi); AFM images were taken by a Bruker Multimode8 AFM system; The Raman spectra are measured by Raman spectrometer (Horiba Jobin Yvon HR Evolution, the excitation light source is a 532 nm laser). The UV–vis optical spectra are measured by ultraviolet visible spectrophotometer (UV 2450, Shimadzu).

SHG Measurement
The SHG laser pulse duration was 10 s, and the laser spot was 1 µm × 1 µm. The fundamental frequency signal is focused onto the sample by using an pulsed laser. A long-pass dichroic mirror separates the reflected fundamental signal from the second harmonic signal. The SHG is directed onto a tube lens and projected onto a CCD camera, forming the image of the SHG signal.

Results and Discussion
As studied, the Cs_3BiBr_6 presents a monoclinic phase at room temperature, and the corresponding space group is C2/c, whose lattice parameters are: $a = 28.31$ Å, $b = 8.617$ Å, $c = 13.71$ Å, $\beta = 99.48°$, unit cell volume = 329.8 Å^3 (Fig. 1a left) [47]. Notably, the $[BiBr_6]^{3-}$ regular octahedrons are isolated from each other and disconnected from the vertex bromine atoms (Fig. 1a right), resulting in electrons and holes localized in the $[BiBr_6]^{3-}$ octahedrons. Therefore, it is usually defined as the zero-dimensional structure. Herein, a solvent evaporation crystallization strategy is adopted to grow the thin films. Briefly, CsBr and $BiBr_3$ are dissolved in dimethyl sulfoxide. Then, a drop of precursor solution is dropped onto clean substrate accompanying with being heated to evaporate the solvent. As the solution reaches supersaturation, the nucleation and growth process were occurred. Finally, the well-defined thin films can be synthesized on the substrate (the synthesis process is illustrated in

Fig. 1 **a** Schematic diagram of the Cs_3BiBr_6 zero-dimensional structure: top view (left) and side view (right). **b** Schematic procedure of Cs_3BiBr_6 film growth. **c** Optical microscope image of the obtained Cs_3BiBr_6 films. **d** Height profile obtained from the AFM profile image of the Cs_3BiBr_6 film in (**c**). **e** XRD patterns of the Cs_3BiBr_6 and Cs_3BiCl_6 films. **f** Optical microscope image of the obtained Cs_3BiCl_6 films. **g** Height profile obtained from the AFM profile image of the Cs_3BiBr_6 film in (**f**). **h** Raman spectra of the Cs_3BiBr_6 and Cs_3BiCl_6 films
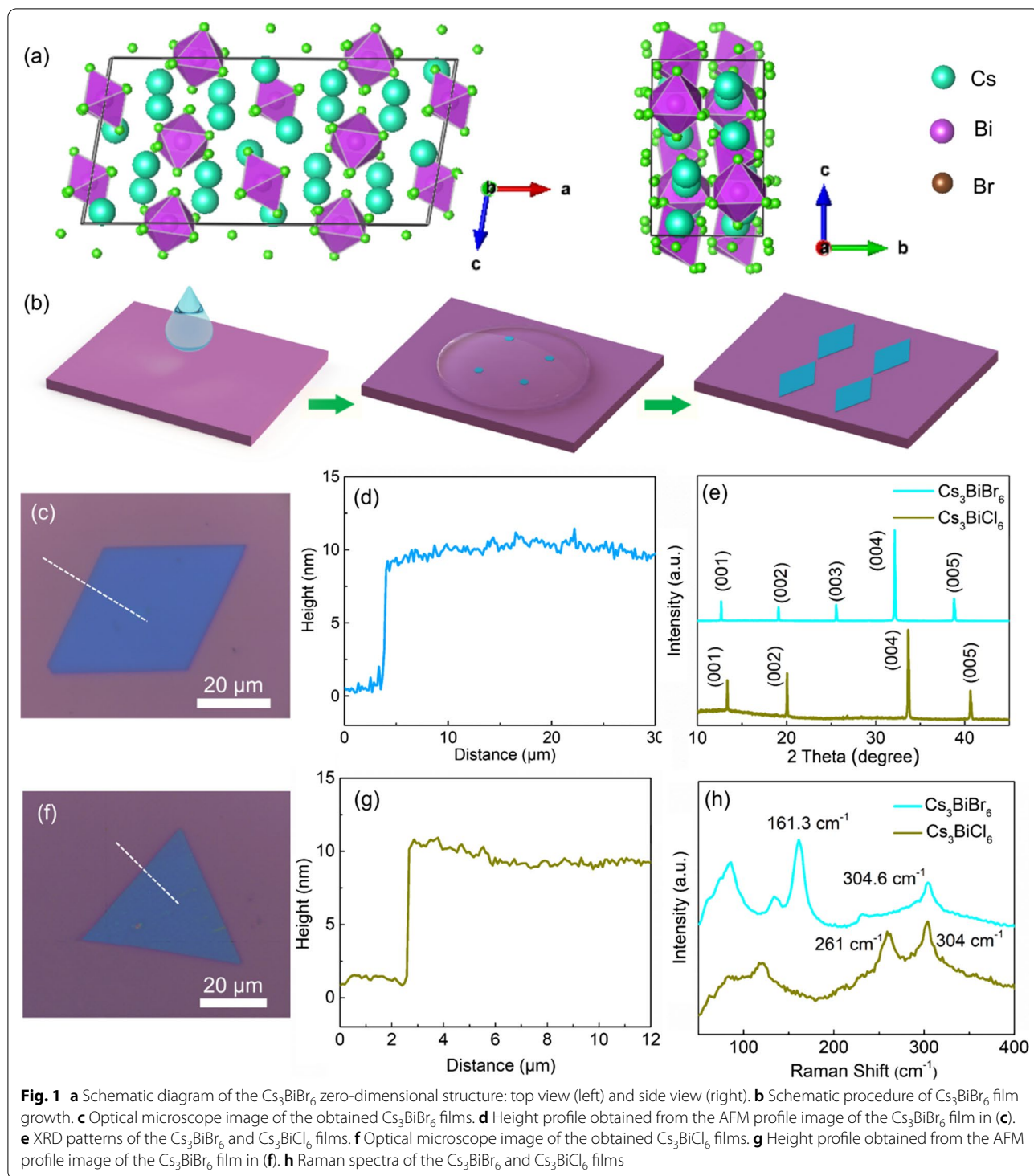
Fig. 1b, and the details are described in experimental section).

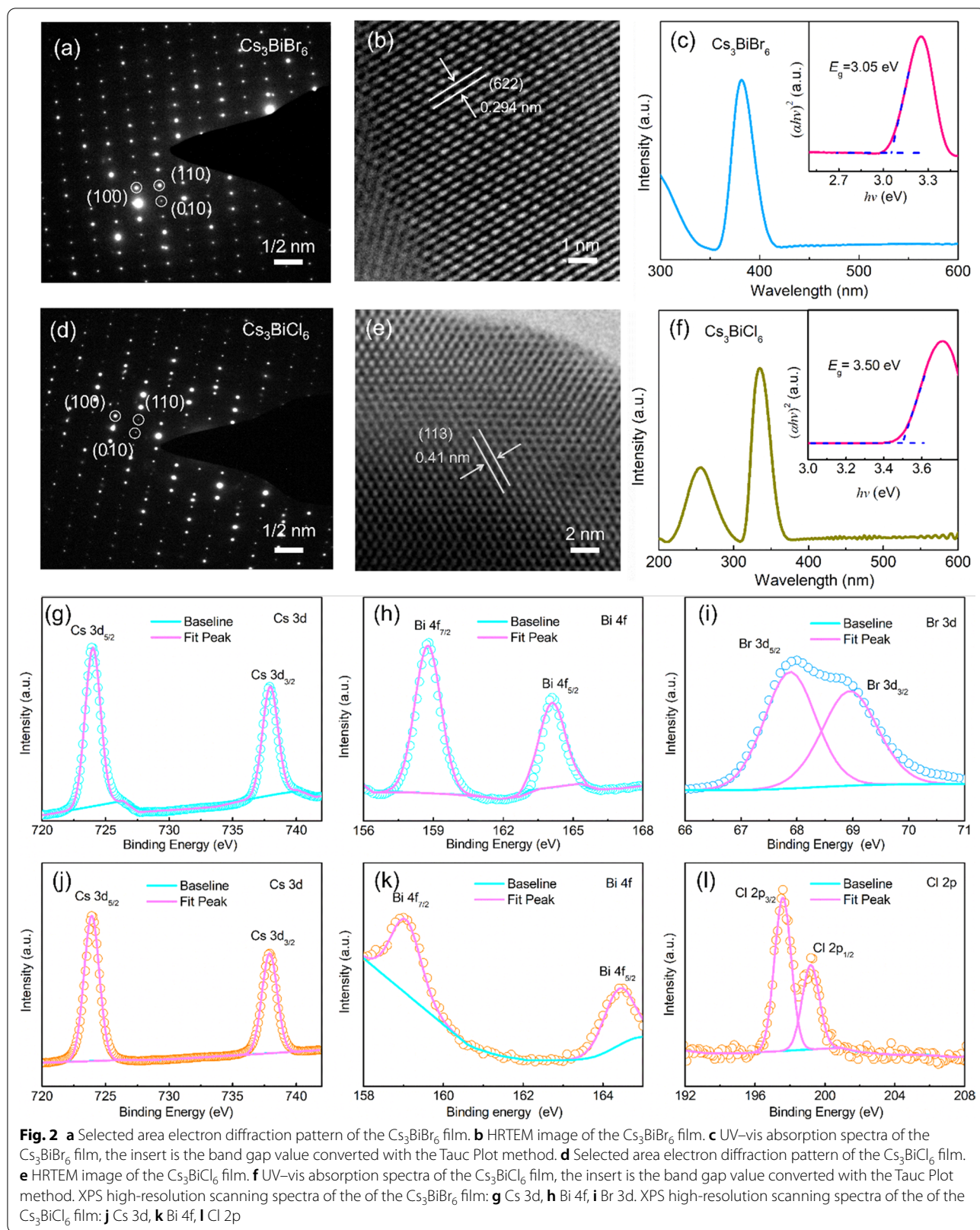The morphology of the film is investigated by optical microscope. As shown in Fig. 1c, regular rhombus morphology with four long sides is observed on the Si/SiO$_2$ substrate. The film shows blue color, while the thickness of film is estimated to be around 9 nm by atomic force microscopy (Fig. 1d). As the precursor metal halide salts changed from -Br to -Cl, the counterparts Cs_3BiCl_6 films with thickness of about 9 nm exhibit the morphology

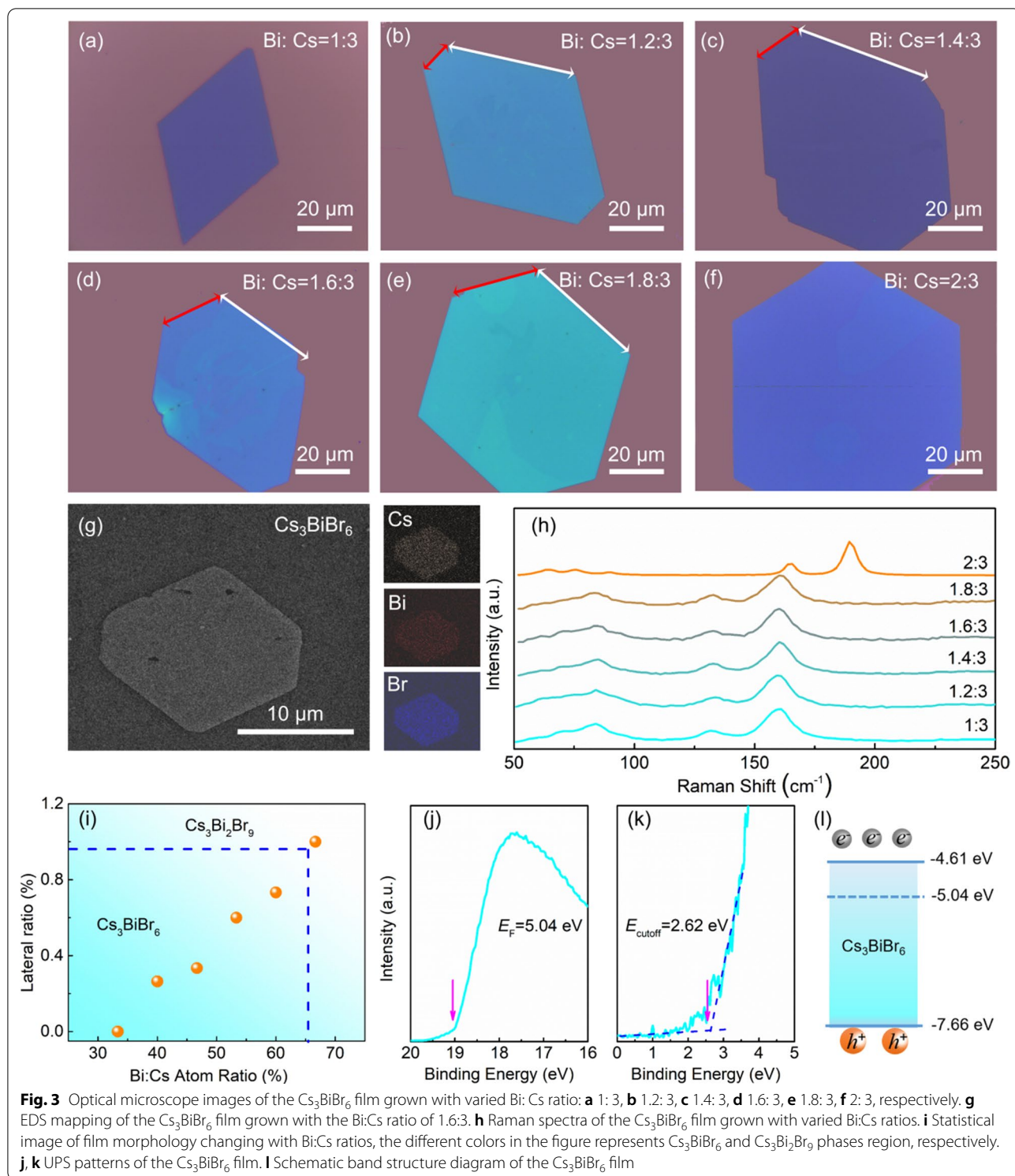Yao *et al. Nanoscale Research Letters*   (2022) 17:115

Page 4 of 9

varying from regular rhombus to regular triangle and hexagon (Fig. 1f and g). To identify their crystal structures, the x-ray diffraction (XRD) patterns were obtained, as shown in Fig. 1e. The Br component related sample shows five clear and sharp peaks located at 12.69°, 19.12°, 25.56°, 32.13°, and 38.84°, corresponding to the (400), (600), (800), (1000), and (1200) facets, respectively. Reasonably, the periodic diffraction peaks can indicate good orientation of Cs_3BiBr_6. According to the Bragg diffraction formula: $2d \cdot \sin\theta = n\lambda$, where the θ is half of the diffraction peaks position ($\theta = 6.345°$), λ is the wavelength of the Cu Kα (1.5406 Å), the lattice spacing is calculated to be ~6.97 Å. This parameter agrees well with the theoretical value of 7.07 Å. Similarly, the sample containing Cl component presents the clear peaks located at 13.367°, 20.047°, 33.655°, 40.655°, and 47.365°, corresponding to the (400), (600), (1000), (1200), and (1400) facets of Cs_3BiCl_6, respectively. Compared with the Cs_3BiBr_6 sample, all the peaks of Cs_3BiCl_6 are moved toward higher diffraction angles. It is result from the smaller atomic radius of Cl that induced smaller lattice parameters and spacing. Moreover, the lattice spacing can be calculated to be ~6.695 Å by the Bragg diffraction formula. Furthermore, the Raman spectroscopy was employed to investigate phonon oscillation of the film. As shown in Fig. 1g, two clear vibration peaks of Cs_3BiBr_6 resolved at 304.6 cm^{-1} and 161.3 cm^{-1} are attributed to $[BiBr_6]^{3-}$ complexes. Since the $[BiBr_6]^{3-}$ is not corner shared, the vibration peaks present asymmetric broadening. At the same time, the Raman spectrum of Cs_3BiCl_6 show the two broad peaks around 261 cm^{-1} and 304 cm^{-1} (Fig. 1g), similar to the Cs_3BiBr_6 sample.

To further investigate the microstructure and crystallization of the film, Fig. 2a shows the Selected Area Electron Diffraction (SAED) pattern of the Cs_3BiBr_6 sample. The clear lattice image without diffractive ring was observed, suggesting the single crystalline features in the local area. The diffraction spots can be labelled (100), (110), and (010) facets, respectively. Figure 2b presents the high-resolution TEM (HRTEM) with clear and long range order lattice It is measured to be ~0.294 nm, corresponding to the (622) facet of the Cs_3BiBr_6. Due to the different atomic radius, the SAED pattern of Cs_3BiCl_6 presents more obvious zero-dimensional structure features whose diffraction intensity periodically changes along the same crystal orientation axis (Fig. 2d). Simultaneously, the HRTEM of Cs_3BiCl_6 in Fig. 2e shows the lattice fringe spacing of ~0.41 nm, corresponding to the (113) facet. Furthermore, the optical absorption is a very important feature for Cs_3BiX_6 single crystal films. In terms of Cs_3BiBr_6, Fig. 2c shows a sharp cutoff edge at around 415 nm and a strong absorption peak at around 381 nm. Reasonably, the excitation adsorption feature

of the Cs_3BiBr_6 addresses a direct bandgap semiconductor with the bandgap value of ~3.05 eV via the Tauc plot method (Fig. 2c insert). As for the Cs_3BiCl_6 single crystal film, it shows a sharp cutoff edge at around 370 nm and a strong excitation adsorption peak central at around 335 nm in Fig. 2f, indicating a direct bandgap semiconductor feature with the bandgap value of ~3.5 eV via the Tauc Plot method (Fig. 2f insert). The calculated bandgap of Cs_3BiX_6 films agree well with the previous Cs_3BiX_6 quantum dots in the literature [47]. To investigate the element valance state, Fig. 2g–i shows the XPS high-resolution scanning spectra of the Cs_3BiBr_6 single crystal film. The binding energy located at 158.8 eV and 164.1 eV for Bi 4f, 723.96 eV and 737.95 eV for Cs 3d, 67.89 eV and 68.96 eV for Br 2p can be assigned to be the Cs^+, Bi^{3+}, and Cl^-, respectively. Meanwhile, Fig. 2j–l shows the binding energy located at 159 eV and 164.4 eV for Bi 4f, 724.3 eV and 738.2 eV for Cs 3d, 197.5 eV and 199.2 eV for Cl 2p, corresponding to the Cs^+, Bi^{3+}, and Cl^- of the Cs_3BiCl_6 single crystal film, respectively. Compared with the Br component sample, the XPS high-resolution spectra of Bi 4f and Cs 3d in Cl component sample have more obvious shift toward higher binding energy. It can be due to the shorter bond length and stronger bond energy than the Br component sample, and the change in valence state is consistent with the slight difference in their intrinsic structure.

Apart from the Cs_3BiBr_6 components, it is noticed that the cesium bismuth halide compounds have another phase $Cs_3Bi_2Br_9$ with higher $BiBr_3$ stoichiometric ratio and another crystal structure. To further study the evolution and control mechanism of the two-phase, more systematic experiments were carried out, including varying proportions of Bi: Cs in the precursor. As the percent of Bi:Cs is changed from 33 to 60% in Fig. 3a–f, the shape of the film shows obvious transformation from the initial rhombus with four sides to the following hexagon along with the two edge length increased. As well known, the concentration has a huge influence on chemical potential, thus it could suggest that the chemical potential of Bi plays a significant role during the film morphology transformation from rhombus toward hexagon. In addition, Fig. 3g illustrates energy dispersion spectroscopy mapping results of the samples. Cs, Bi and Br elements in the samples are distinguished and distributed uniformly, which could be estimated to be the elements proportion of 2.6: 1: 7.1. The ratio is close to the Cs_3BiBr_6 phase. The Raman spectroscopy measurement is used to further evaluate the composition. In Fig. 3h, when the ratio is below 2:3, the peak intensity and wavenumber of the peaks resolved around 160 cm^{-1} and 132 cm^{-1} did not show evident difference among the samples. This indicates that the morphological variation should be not

Yao *et al. Nanoscale Research Letters*   (2022) 17:115

Page 5 of 9

Fig. 2 **a** Selected area electron diffraction pattern of the Cs_3BiBr_6 film. **b** HRTEM image of the Cs_3BiBr_6 film. **c** UV–vis absorption spectra of the Cs_3BiBr_6 film, the insert is the band gap value converted with the Tauc Plot method. **d** Selected area electron diffraction pattern of the Cs_3BiCl_6 film. **e** HRTEM image of the Cs_3BiCl_6 film. **f** UV–vis absorption spectra of the Cs_3BiCl_6 film, the insert is the band gap value converted with the Tauc Plot method. XPS high-resolution scanning spectra of the of the Cs_3BiBr_6 film: **g** Cs 3d, **h** Bi 4f, **i** Br 3d. XPS high-resolution scanning spectra of the of the Cs_3BiCl_6 film: **j** Cs 3d, **k** Bi 4f, **l** Cl 2p

Yao *et al. Nanoscale Research Letters*   (2022) 17:115

Page 6 of 9

Fig. 3 Optical microscope images of the Cs_3BiBr_6 film grown with varied Bi: Cs ratio: **a** 1: 3, **b** 1.2: 3, **c** 1.4: 3, **d** 1.6: 3, **e** 1.8: 3, **f** 2: 3, respectively. **g** EDS mapping of the Cs_3BiBr_6 film grown with the Bi:Cs ratio of 1.6:3. **h** Raman spectra of the Cs_3BiBr_6 film grown with varied Bi:Cs ratios. **i** Statistical image of film morphology changing with Bi:Cs ratios, the different colors in the figure represents Cs_3BiBr_6 and $Cs_3Bi_2Br_9$ phases region, respectively. **j**, **k** UPS patterns of the Cs_3BiBr_6 film. **l** Schematic band structure diagram of the Cs_3BiBr_6 film

accompanied with structure phase transition. Furthermore, as the Bi:Cs further rise to 2:3 (67%), the $Cs_3Bi_2Br_9$ phase can dominate crystallization process, while two-phase coexistence phenomenon cannot be found based

on the Raman spectra. Reasonably, it should be due to the higher forming energy barrier of $Cs_3Bi_2Br_9$ phase. Consequently, the phase and lateral size as a function of Bi proportion is extracted and statistics in Fig. 3i, it exhibiting

obvious chemical potential dependency on BiBr₃. Furthermore, the detailed band structure of the Cs₃BiBr₆ is investigated from ultraviolet photoelectron spectroscopy (Fig. 3j and k), and the Fermi level and E_{cutoff} are − 5.04 eV and 2.62 eV, respectively. The valance band maximum and conduct band minimum are estimated to be − 7.66 eV and − 4.61 eV, respectively (as illustrated in Fig. 3l). As shown, the Fermi level is close to conduct band bottom, suggesting n-type semiconductor features.

Considering the crystal structure of Cs₃BiBr₆ exhibiting spatial symmetry, lattice parameters (such as bond length and bond angle) could change as the thickness decreased down to atomic level and morphology transition. To further identify the above cases, the second harmonic generation (SHG) measurements for the Cs₃BiBr₆ film were performed. A 1064 nm laser is used as excitation light source. Firstly, no SHG signal is observed in the thick film (about 640 nm) of the rhombus sample, while the region with smaller thickness film (about 39 nm) shows SHG signals (Fig. 4a and b). In addition, for the Cs₃BiBr₆ hexagonal film, as shown in Fig. 4c, there is a doubling frequency signal at 532 nm and the intensity

is regularly increased as the laser power increasing from 25.8 mW to 133.2 mW. Figure 4d shows the statistics result of SHG intensity as a function of laser power, illustrating the linear relationship with a slop of 0.81 by a parabolic relationship ($I \propto P^{\theta}$). According to the electric dipole approximation theory [51], the second harmonic signal can be only generated in the medium with asymmetric center. Therefore, it indicates that there is an obvious lattice parameter variation, forming an asymmetric structure in the film. To sum up, as the dimensionality of Cs₃BiBr₆ is decreased or shape changed to hexagonal), symmetry can tend to be easily broken. This work might provide a thought about the growth of low-dimensional materials and show further influence on electron/band structures.

Conclusion

In conclusion, we report the successful growth of zero-dimensional Cs₃BiX₆ (X = Br, Cl) single crystal films with a solvent evaporation crystallization strategy. It was found that solution concentration is strongly correlated with chemical potential, which plays a key role
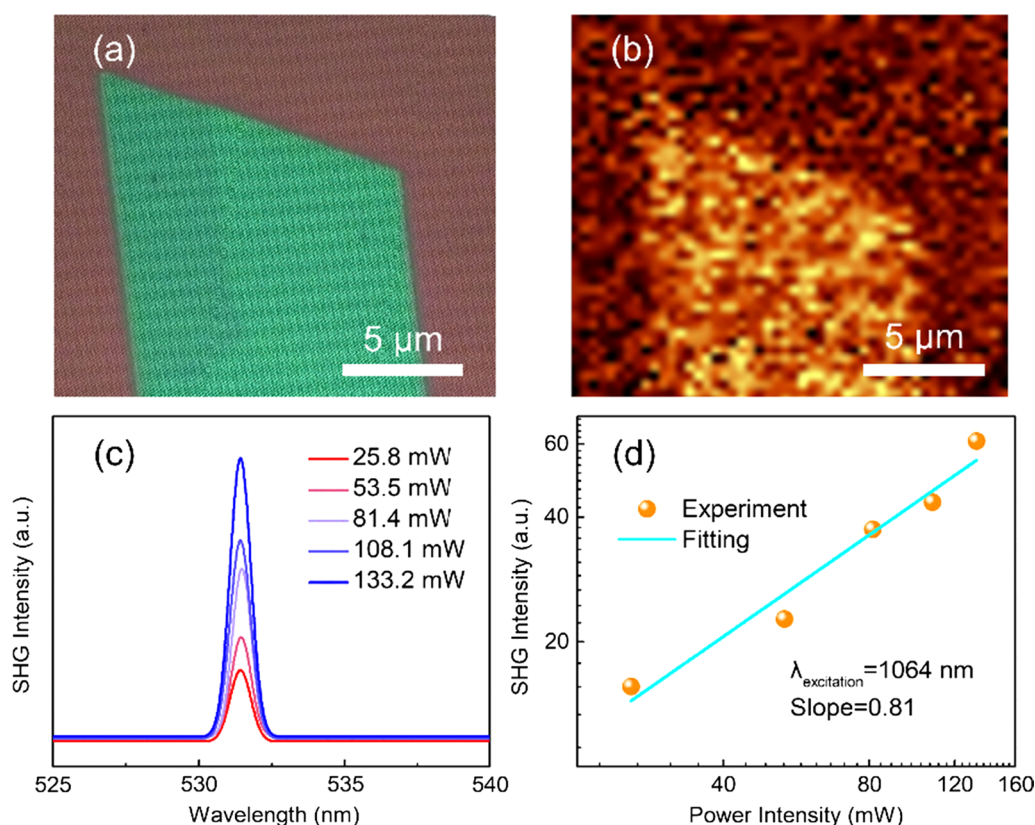

Fig. 4 **a** Optical microscope image of the Cs₃BiBr₆ film that used for SHG measurement. **b** SHG mapping image of the rhombus sample in (**a**). **c** Second harmonic generation properties of the Cs₃BiBr₆ film with varied excitation power. **d** Statistical image of SHG intensity as a function of excitation power intensities

Yao *et al. Nanoscale Research Letters* (2022) 17:115

Page 8 of 9

on morphology evolution from rhombus to hexagon. A robust second harmonic generation signal demonstrates the broken symmetry, attributed to decreased dimension or shape change. This work not only provides a single crystal film growth method for zero-dimensional structural materials, but also conducive to understanding the electron and band structure change as its thickness reduced.

Author Contributions
Authors GZ and YC conceived the idea. JY, ZZ, and LL prepared all the samples and did the major characterizations. YS and XW contributes to the characterization of TEM. CW, ZB, and QZ contribute to the SHG analysis. HX, ZL, and HX provide supporting on structural analysis and language expression revision. YC and GZ discussed the results, analyzed the data, and co-wrote this manuscript. All authors reviewed the manuscript.

Availability of Data and Materials
All datasets are presented in the main paper and freely available to any scientist wishing to use them for non-commercial purposes, without breaching participant confidentiality.

Declarations

Ethics Approval and Consent to Participate
Not applicable.

Consent for Publication
Not applicable.

Competing interests
The authors declare that they have no competing interests.

Author details
[1]School of Energy, Key Laboratory of Advanced Carbon Materials and Wearable Energy Technologies of Jiangsu Province, Soochow University, Suzhou 215006, People's Republic of China. [2]College of Mechanical and Electronic Engineering, Shandong University of Science and Technology, Qingdao 266590, People's Republic of China. [3]School of Physics, University of Electronic Science and Technology of China, Chengdu 610054, People's Republic of China. [4]Yangtze Delta Region Institute (Huzhou), University of Electronic Science and Technology of China, Huzhou 313001, People's Republic of China.

References
1. Saidaminov MI, Mohammed OF, Bakr OM (2017) Low-dimensional-networked metal halide perovskites: the next big thing. ACS Energy Lett 2:889
2. Ju M-G, Dai J, Ma L, Zhou Y, Zeng XC (2018) Zero-dimensional organic-inorganic perovskite variant: transition between molecular and solid crystal. J Am Chem Soc 140:10456
3. Leng K, Abdelwahab I, Verzhbitskiy I, Telychko M, Chu L, Fu W, Chi X, Guo N, Chen Z, Chen Z, Zhang C, Xu QH, Lu J, Chhowalla M, Eda G, Loh KP (2018) Molecularly thin two-dimensional hybrid perovskites with tunable optoelectronic properties due to reversible surface relaxation. Nat Mater 17:908
4. Li Z, Liu X, Zuo C, Yang W, Fang X (2021) Supersaturation-controlled growth of monolithically integrated lead-free halide perovskite single-crystalline thin film for high-sensitivity photodetectors. Adv Mater 33:e2103010
5. Chen W, Deng Z, Guo D, Chen Y, Mazur YI, Maidaniuk Y, Benamara M, Salamo GJ, Liu H, Wu J, Chen B (2018) Demonstration of InAs/InGaAs/GaAs quantum dots-in-a-well mid-wave infrared photodetectors grown on silicon substrate. J Lightwave Technol 36:2572
6. Guo D, Jiang Q, Tang M, Chen S, Mazur YI, Maidaniuk Y, Benamara M, Semtsiv MP, Masselink WT, Salamo GJ, Liu H, Wu J (2018) Two-colour In$_{0.5}$Ga$_{0.5}$As quantum dot infrared photodetectors on silicon. Semicond Sci Tech 33:094009
7. Xu H, Han X, Dai X, Liu W, Wu J, Zhu J, Kim D, Zou G, Sablon KA, Sergeev A, Guo Z, Liu H (2018) High detectivity and transparent few-layer MoS$_2$/glassy-graphene heterostructure photodetectors. Adv Mater 30:e1706561
8. Yang P, Zhang Z, Sun M, Lin F, Cheng T, Shi J, Xie C, Shi Y, Jiang S, Huan Y, Liu P, Ding F, Xiong C, Xie D, Zhang Y (2019) Thickness tunable wedding-cake-like mos$_2$ flakes for high-performance optoelectronics. ACS Nano 13:3649
9. Withers F, Del Pozo-Zamudio O, Mishchenko A, Rooney AP, Gholinia A, Watanabe K, Taniguchi T, Haigh SJ, Geim AK, Tartakovskii AI, Novoselov KS (2015) Light-emitting diodes by band-structure engineering in van der Waals heterostructures. Nat Mater 14:301
10. Yang W, Shang J, Wang J, Shen X, Cao B, Peimyoo N, Zou C, Chen Y, Wang Y, Cong C, Huang W, Yu T (2016) Electrically tunable valley-light emitting diode (vLED) based on CVD-grown monolayer WS$_2$. Nano Lett 16:1560
11. Wu S, Buckley S, Schaibley JR, Feng L, Yan J, Mandrus DG, Hatami F, Yao W, Vuckovic J, Majumdar A, Xu X (2015) Monolayer semiconductor nanocavity lasers with ultralow thresholds. Nature 520:69
12. Shi Y, Liang X, Yuan B, Chen V, Li H, Hui F, Yu Z, Yuan F, Pop E, Wong HSP, Lanza M (2018) Electronic synapses made of layered two-dimensional materials. Nat Electron 1:458
13. Wang M, Cai S, Pan C, Wang C, Lian X, Zhuo Y, Xu K, Cao T, Pan X, Wang B, Liang S-J, Yang JJ, Wang P, Miao F (2018) Robust memristors based on layered two-dimensional materials. Nat Electron 1:130
14. Ciarrocchi A, Avsar A, Ovchinnikov D, Kis A (2018) Thickness-modulated metal-to-semiconductor transformation in a transition metal dichalcogenide. Nat Commun 9:919
15. Zhang S, Yan Z, Li Y, Chen Z, Zeng H (2015) Atomically thin arsenene and antimonene: semimetal-semiconductor and indirect-direct band-gap transitions. Angew Chem Int Ed 54:3112
16. Wang H, Huang X, Lin J, Cui J, Chen Y, Zhu C, Liu F, Zeng Q, Zhou J, Yu P, Wang X, He H, Tsang SH, Gao W, Suenaga K, Ma F, Yang C, Lu L, Yu T, Teo EHT, Liu G, Liu Z (2017) High-quality monolayer superconductor NbSe$_2$ grown by chemical vapour deposition. Nat Commun 8:394
17. Cheema SS, Kwon D, Shanker N, Dos Reis R, Hsu SL, Xiao J, Zhang H, Wagner R, Datar A, McCarter MR, Serrao CR, Yadav AK, Karbasian G, Hsu CH, Tan AJ, Wang LC, Thakare V, Zhang X, Mehta A, Karapetrova E, Chopdekar RV, Shafer P, Arenholz E, Hu C, Proksch R, Ramesh R, Ciston J, Salahuddin S (2020) Enhanced ferroelectricity in ultrathin films grown directly on silicon. Nature 580:478
18. Huang B, Clark G, Navarro-Moratalla E, Klein DR, Cheng R, Seyler KL, Zhong D, Schmidgall E, McGuire MA, Cobden DH, Yao W, Xiao D, Jarillo-Herrero P, Xu X (2017) Layer-dependent ferromagnetism in a van der Waals crystal down to the monolayer limit. Nature 546:270
19. Zhang Y, Tan YW, Stormer HL, Kim P (2005) Experimental observation of the quantum Hall effect and Berry's phase in graphene. Nature 438:201
20. Zhou J, Lin J, Huang X, Zhou Y, Chen Y, Xia J, Wang H, Xie Y, Yu H, Lei J, Wu D, Liu F, Fu Q, Zeng Q, Hsu CH, Yang C, Lu L, Yu T, Shen Z, Lin H, Yakobson BI, Liu Q, Suenaga K, Liu G, Liu Z (2018) A library of atomically thin metal chalcogenides. Nature 556:355

21. Zhou J, Zhu C, Zhou Y, Dong, Li P, Zhang Z, Wang Z, Lin YC, Shi J, Zhang R, Zheng Y, Yu H, Tang B, Liu F, Wang L, Liu L, Liu GB, Hu W, Gao Y, Yang H, Gao W, Lu L, Wang Y, Suenaga K, Liu G, Ding F, Yao Y, Liu Z (2022) Composition and phase engineering of metal chalcogenides and phosphorous chalcogenides. Nat Mater. https://doi.org/10.1038/s41563-022-01291-5

22. Li L, Yu Y, Li P, Liu J, Liang L, Wang L, Ding Y, Han X, Ji J, Chen S, Li D, Liu P, Zhang S, Zeng M, Fu L (2022) The universal growth of ultrathin perovskite single crystals. Adv Mater 34:e2108396

23. Ren A, Wang H, Zhang W, Wu J, Wang Z, Penty RV, White IH (2021) Emerging light-emitting diodes for next-generation data communications. Nat Electron 4:559

24. Xu H, Ren A, Wu J, Wang Z (2020) Recent advances in 2D MXenes for photodetection. Adv Funct Mater 30:2000907

25. Shi D, Adinolfi V, Comin R, Yuan MJ, Alarousu E, Buin A, Chen Y, Rothenberger SH, Katsiev K, Losovyj Y, Zhang X, Dowben PA, Mohammed OF, Sargent EH, Bakr OM (2015) Low trap-state density and long carrier diffusion in organolead trihalide perovskite single crystals. Science 347:519

26. Akkerman QA, Motti SG, Kandada ARS, Mosconi E, Innocenzo VD, Bertoni G, Marras S, Kamino BA, Miranda L, Angelis FD, Petrozza A, Prato M, Manna L (2016) Solution synthesis approach to colloidal cesium lead halide perovskite nanoplatelets with monolayer-level thickness control. J Am Chem Soc 138:1010

27. Protesescu L, Yakunin S, Bodnarchuk MI, Krieg F, Caputo R, Hendon CH, Yang RX, Walsh A, Kovalenko MV (2015) Nanocrystals of cesium lead halide perovskites (CsPbX(3), X = Cl, Br, and I): novel optoelectronic materials showing bright emission with wide color gamut. Nano Lett 15:3692

28. Kojima A, Teshima K, Shirai Y, Miyasaka T (2009) Organometal halide perovskites as visible-light sensitizers for photovoltaic cells. J Am Chem Soc 131:6050

29. Leng M, Chen Z, Yang Y, Li Z, Zeng K, Li K, Niu G, He Y, Zhou Q, Tang J (2016) Lead-free, blue emitting bismuth halide perovskite quantum dots. Angew Chem Int Ed 55:15012

30. Locardi F, Cirignano M, Baranov D, Dang Z, Prato M, Drago F, Ferretti M, Pinchetti V, Fanciulli M, Brovelli S, De Trizio L, Manna L (2018) Colloidal synthesis of double perovskite $Cs_2AgInCl_6$ and Mn-doped $Cs_2AgInCl_6$ nanocrystals. J Am Chem Soc 140:12989

31. Zhu H, Fu Y, Meng F, Wu X, Gong Z, Ding Q, Gustafsson MV, Trinh MT, Jin S, Zhu XY (2015) Lead halide perovskite nanowire lasers with low lasing thresholds and high quality factors. Nat Mater 14:636

32. Chen J, Fu Y, Samad L, Dang L, Zhao Y, Shen S, Guo L, Jin S (2017) Vapor-phase epitaxial growth of aligned nanowire networks of cesium lead halide perovskites (CsPbX$_3$, X = Cl, Br, I). Nano Lett 17:460

33. Dou LT, Lai ML, Kley CS, Yang YM, Bischak CG, Zhang DD, Eaton SW, Ginsberg NS, Yang PD (2017) Spatially resolved multicolor CsPbX$_3$ nanowire heterojunctions via anion exchange. Proc Natl Acad Sci USA 114:7216

34. Chen YX, Ge QQ, Shi Y, Liu J, Xue DJ, Ma JY, Ding J, Yan HJ, Hu JS, Wan LJ (2016) General space-confined on-substrate fabrication of thickness-adjustable hybrid perovskite single-crystalline thin films. J Am Chem Soc 138:16196

35. Chen Z, Dong Q, Liu Y, Bao C, Fang Y, Lin Y, Tang S, Wang Q, Xiao X, Bai Y, Deng Y, Huang J (1890) Thin single crystal perovskite solar cells to harvest below-bandgap light absorption. Nat Commun 2017:8

36. Bekenstein Y, Koscher BA, Eaton SW, Yang P, Alivisatos AP (2015) Highly luminescent colloidal nanoplates of perovskite cesium lead halide and their oriented assemblies. J Am Chem Soc 137:16008

37. Dou LT, Wong AB, Yu Y, Lai ML, Kornienko N, Eaton SW, Fu A, Bischak CG, Ma J, Ding T, Ginsberg NS, Wang LW, Alivisatos AP, Yang Pd (2015) Atomically thin two-dimensional organic-inorganic hybrid perovskites. Science 349:1518

38. Huo C, Cai B, Yuan Z, Ma B, Zeng H (2017) Two-dimensional metal halide perovskites: theory, synthesis, and optoelectronics. Small Methods 1:1600018

39. Li J, Wang J, Ma J, Shen H, Li L, Duan X, Li D (2019) Self-trapped state enabled filterless narrowband photodetections in 2D layered perovskite single crystals. Nat Commun 10:806

40. Gao Y, Shi E, Deng S, Shiring SB, Snaider JM, Liang C, Yuan B, Song R, Janke SM, Liebman-Pelaez A, Yoo P, Zeller M, Boudouris BW, Liao P, Zhu C, Blum V, Yu Y, Savoie BM, Huang L, Dou L (2019) Molecular engineering of organic-inorganic hybrid perovskites quantum wells. Nat Chem 11:1151

41. Cheng L, Jiang T, Cao Y, Yi C, Wang N, Huang W, Wang J (2019) Multiple-quantum-well perovskites for high-performance light-emitting diodes. Adv Mater 32:e1904163

42. Bekenstein Y, Dahl JC, Huang J, Osowiecki WT, Swabeck JK, Chan EM, Yang P, Alivisatos AP (2018) The making and breaking of lead-free double perovskite nanocrystals of cesium silver-bismuth halide compositions. Nano Lett 18:3502

43. Fan QQ, Biesold-McGee GV, Xu QN, Pan S, Peng J, Ma JZ, Lin ZQ (2020) Lead-free halide perovskite nanocrystals: crystal structures, synthesis, stabilities, and optical properties. Angew Chem Int Ed 59:1030

44. McCall KM, Stoumpos CC, Kontsevoi OY, Alexander GCB, Wessels BW, Kanatzidis MG (2019) From 0D $Cs_3Bi_2I_9$ to 2D $Cs_3Bi_2I_6Cl_3$: dimensional expansion induces a direct band gap but enhances electron-phonon coupling. Chem Mater 31:2644

45. Yang B, Chen JS, Hong F, Mao X, Zheng KB, Yang SQ, Li YJ, Pullerits T, Deng WQ, Han KL (2017) Lead-free, air-stable all-inorganic cesium bismuth halide perovskite nanocrystals. Angew Chem Int Ed 56:12471

46. Zhang Y, Liu Y, Xu Z, Ye H, Yang Z, You J, Liu M, He Y, Kanatzidis MG, Liu SF (2020) Nucleation-controlled growth of superior lead-free perovskite $Cs_3Bi_2I_9$ single-crystals for high-performance X-ray detection. Nat Commun 11:2304

47. Yang H, Cai T, Liu E, Hills-Kimball K, Gao J, Chen O (2019) Synthesis and transformation of zero-dimensional Cs_3BiX_6 (X = Cl, Br) perovskite-analogue nanocrystals. Nano Res 13:282

48. Creutz SE, Liu H, Kaiser ME, Li X, Gamelin DR (2019) Structural diversity in cesium bismuth halide nanocrystals. Chem Mater 31:4685

49. Shimizu M, Koshimizu M, Fujimoto Y, Yanagida T, Ono S, Asai K (2016) Luminescence and scintillation properties of Cs_3BiCl_6 crystals. Opt Mater 61:115

50. Tang Y, Liang M, Chang B, Sun H, Zheng K, Pullerits T, Chi Q (2019) Lead-free double halide perovskite Cs_3BiBr_6 with well-defined crystal structure and high thermal stability for optoelectronics. J Mater Chem C 7:3369

51. Shimizu A (1988) Optical nonlinearity induced by giant dipole moment of Wannier excitons. Phys Rev Lett 61:613

Publisher's Note